Numerical Prediction of Flow in Swirl Chamber of Diesel Engines

G. Komatsu and M. Takata
Department of Mechanical Engineering
Himeji Institute of Technology
Shosha 2167, Himeji 671-22

ABSTRACT

Flow prediction and measurement were performed to clarify swirl chamber flow in diesel engines. A flow model is based on the solution of the finite difference form of the governing differential equations for the transport of mass, momentum, kinetic energy of turbulence, and its dissipation rate. Simulations have been made using flow models for the three kinds of swirl chambers with different connecting passages. Before predicting swirl chamber flow, the flow model was confirmed in experiments using an air model. Then flow characteristics in the swirl chamber of a full scale engine were predicted. Swirl chamber geometry was found to extensively influence basic flow characteristics, such as tangential velocity and turbulence intensity.

INTRODUCTION

Air flow in the swirl chamber of diesel engines greatly influences the fuel-air mixing and combustion processes. They also affect noise emission and the formation of pollutants such as soot and nitrous oxides. Swirl produced during compression has great influence on mixture formation and subsequent combustion. Air flow during expansion stroke is also important in that it ensures final air utilization in the main chamber. Numerous efforts have therefore been made to clarify swirl chamber flow characteristics. However, many results are not quantitative but qualitative, resulting in a limited understanding at present.

To arrive at a better understanding, a flow prediction method should be established using the modern computer prediction method developed by the following investigators. Gosman and his coworkers (1) and Ramos et al (2) solved flows in the engine cylinder using the finite difference method. Elkotb et al (3) used this same technique to assess swirl chamber flow in diesel engines. Several three-dimensional simulations have been presented recently by Ikegami and his coworkers (4), Nishiwaki et al (5), and Wakisaka et al (6). Their results suggested that the method is suitable for predicting swirl production.

In this study, the authors aimed to understand swirl chamber flow using a similar approach. Special emphasis was placed on the effects of swirl chamber geometry and the connecting passage. To elucidate combustion in the later crank angles, swirl motion during the expansion stroke was also studied. The k-ε model parameters proposed by Jones and Launder (7) were used in prediction method. Before predicting swirling flow in an actual engine, numerical prediction results were comfirmed in experments using a special air model. Finally, the effects of swirl chamber geometry on flow characteristics were examined under full-scale engine conditions.

FLOW MODEL

To facilitate flow analysis, swirl chamber flow in diesel engines was assumed to be two-dimensional and transient. Turbulent shear stress was expressed as the product of local turbulent effective viscosity and local mean rate of strain. The turbulent effective viscosity was determined according to the turbulent structure related to turbulence kinetic energy k and its dissipation rate ε. Within this framework we adopted the k-ε model proposed by Jones et al.

Flow model. Flow is described in terms of partial differential equations that govern mass continuity and momentum together with the kinetic energy of turbulence k and its dissipation rate ε. Polar coordinates (r,θ) were used. The governing set of equations may be compactly represented in terms of a single general transport equation for an arbitrary dependent variable.

$$\frac{\partial}{\partial t}(\rho\phi) + \frac{1}{r}\frac{\partial}{\partial r}(r\rho u\phi) + \frac{1}{r}\frac{\partial}{\partial \theta}(\rho v\phi) - \frac{1}{r}\frac{\partial}{\partial r}(r\Gamma\phi\frac{\partial \phi}{\partial r})$$

$$- \frac{1}{r^2}\frac{\partial}{\partial \theta}(\Gamma\phi\frac{\partial \phi}{\partial \theta}) = S\phi \qquad (1)$$

Where ϕ is radial velocity u, tangential velocity v, kinetic energy k, and its dissipation rate ε, t is time, and ρ is density, Γ_ϕ and S_ϕ equal the turbulent effective diffusivity coefficients and source or sink terms respectively. Definitions of Γ_ϕ and S_ϕ are given in Table 1. In this Table 1, μ_{eff} equals turbulent effective viscosity;

$$\mu_{eff} = \mu + C_\mu \rho k^2 / \varepsilon \qquad (2)$$

Table 1 Definitions of coefficients appearing in general transport Eq. 1

ϕ	$\Gamma\phi$	$S\phi$
u	μeff	$-\frac{\partial p}{\partial r} + \frac{1}{r}\frac{\partial}{\partial r}(r\,\mu eff\,\frac{\partial u}{\partial r}) + \frac{1}{r}\frac{\partial}{\partial \theta}\{\mu eff\,(\frac{\partial v}{\partial r} - \frac{v}{r})\} + \frac{\rho v^2}{r}$ $- \frac{2\mu eff}{r^2}(u + \frac{\partial v}{\partial \theta}) - \frac{2}{3r}\frac{\partial}{\partial r}\{r(\mu eff\ div(W) + \rho k)\}$
v	μeff	$-\frac{1}{r}\frac{\partial p}{\partial \theta} + \frac{1}{r}\frac{\partial}{\partial r}\{r\,\mu eff\,(\frac{1}{r}\frac{\partial u}{\partial \theta} - \frac{v}{r})\} + \frac{1}{r^2}\frac{\partial}{\partial \theta}\{\mu eff\,(\frac{\partial v}{\partial \theta} + 2u)\}$ $+ \frac{\mu eff}{r}(\frac{1}{r}\frac{\partial u}{\partial \theta} + \frac{\partial v}{\partial r}) - \mu eff\,\frac{v}{r^2} - \rho\frac{uv}{r} - \frac{2}{3}\frac{1}{r}\frac{\partial}{\partial \theta}(\mu eff\ div(W) + \rho k)$
1	0	0
k	$\frac{\mu eff}{\sigma k}$	$G - C_\mu\,\rho\varepsilon$
ε	$\frac{\mu eff}{\sigma \varepsilon}$	$\frac{\varepsilon}{k}(C_1 G - C_2 \rho\varepsilon)$

$$G = \mu eff\,\{2(\frac{1}{r}\frac{\partial v}{\partial \theta} + \frac{u}{r})^2 + 2(\frac{\partial u}{\partial r})^2 + (\frac{1}{r}\frac{\partial u}{\partial \theta} + \frac{\partial v}{\partial r} - \frac{v}{r})^2\} - \frac{2}{3}\,div(W)\,\{\mu eff\ div(W) + \rho k\}$$

where C_μ, C_1, C_2, σ_K, σ_ε, are turbulence model constants, also given in Table 2 and μ is molecular viscosity.

The general transport equation (1) is solved using a finite difference procedure based on a semi-implicid method. The velocity field u, v is solved explicitly in time increments, after which pressure corrections are implicitly made to satisfy equation continuity. The pressure corrections are calculated using a line-by-line double sweep method. Iteration processes were repeated four times, after which the maximum normalized residual became negligible. The hybrid scheme (8) was used to overcome the difficulty encountered at a high convection rate relative to diffusion.

Boundary and initial conditions. Boundary conditions were assumed as follows. No-slip conditions were applied for velocities at walls, which are thermally insulated. The following wall function was used for grid nodes adjacent to the chamber wall. The turbulent shear stress near the wall is

$$\tau w = \begin{cases} \dfrac{K\,C\mu^{1/4}\,\rho\,v\,k^{1/2}}{\ln(E\,\rho\,y\,k^{1/2}\,\bar{\mu}^{-1})} & , y^+ = \rho\,k^{1/2}\,y\,\bar{\mu}^{-1} \geq 11.5 \\ \mu\,\dfrac{v}{y} & , y^+ < 11.5 \end{cases} \qquad (3)$$

where K=0.4 and E=9.0 are constants of wall function and y is distance from wall. Turbulence fluctuations and their dissipation rate were assumed to be zero at the wall.

At the passage connecting the swirl chamber with the main chamber, inlet velocity and density were given for each crank angle according to piston movement.

Table 2 The values of the empirical constants of the k-ε model of turbulence

$C\mu$	C_1	C_2	σk	$\sigma\varepsilon$
0.09	1.55	2.0	1.0	1.3

ENGINE USED IN PREDICTION AND EXPERIMENT

Predictions for swirl chamber geometries were attempted in an engine, specifications of which are shown in Table 3.

Swirl chamber geometry. The three kinds of swirl chamber shown in Fig.1 were used. Type A is cylindrical, similar to the Ricardo Comet III type, and has a tangential connecting passage. Type B is the same as type A except that the connecting passage is offset. Type C has a flat bottom similar to the Ricardo Comet V type and a connecting passage inclined 45 degrees to the bottom surface. All swirl chambers have a diameter D_s of 37mm and a connecting passage width h_p 0.17% the diameter.

The experimental investigation. Before predicting flow in the above chamber, numerical prediction was confirmed in an experiment using a special air model. A four-cycle diesel engine was rebuilt for the air model by exchanging the cylinder head for one without intake and exhaust valves.

For ease of measurement a cylindrical swirl chamber 60 mm in diameter and approximately 1.6 times the size of the original chamber was installed on the new cylinder head. One side of the chamber was made of aclyl material for visual inspection. The compression ratio was 5 : 1 The air model was powered by an electric dynamometer at 250 rpm.

Table 3 Specifications of engine used in prediction and air model

	Engine used in prediction	Air model
Swirl chamber diameter, mm	37	60
Cylinder diameter, mm	95	150
Stroke, mm	110	110
Swirl chamber volume ratio	0.5	0.13
port area ratio	0.02	0.01
Engine speed, rpm	1800	250

To measure air velocity and its turbulence intensity, a 12.7 μm diameter platinum hot-wire probe was inserted into the swirl chamber. The probe was traversed in the specified radial direction of the chamber. In addition, a pressure transducer was fitted to the chamber to measure pressure as shown in Fig.2.

Hot-wire anemometry was performed under constant temperature. Due to changes in air temperature and density, the anemometer did not give correct velocity. Compensation was made based on the equation of Collis & Williams, on reading gained at a proof-duct under atomospheric conditions, and on the thermal equilibrium of the hot-wire with the surrounding air. Turbulence intensity was determined by an ensemble-average method which assumes fluctuation relative to the ensemble-average to be turbulence intensity.

PREDICTION AND EXPERIMENTAL RESULTS

Special air model. Prediction was carried out using a special air model of swirl chamber type A, dimensions for which are shown in Table 3. The computational grid inside the swirl chamber consisted of 20 angular and 10 radial locations on polar coordinates. Computations were conducted at the beginning of the compression stroke and carried out at increments between 0.01 degree and 0.05 degree in crank angle.

Figure 3 shows the resulting velocity field computed during compression and expansion stroke. The tangential velocity at the specified locations $\ell - \ell'$ shown in Fig.1 are shown in Fig.4. As may be seen in Fig.3 and Fig.4, a radial flow is directed from the connecting passage to the opposite wall at the beginning of compression. A vortex is observed at the left hand side near the connecting passage at a crank angle of about 30 degrees. Later total swirling flow builds up. The increase of inflow to the swirl chamber produces a large tangential velocity, which reaches maximum value at 150 deg.CA during compression stroke, after which it decreases slightly. This may be attributted to the decrease of the ejected velocity from the maximum value at about 150 deg.CA to zero value at TDC. At the end of compression, swirl chamber flow consists of two zones, the rigid-body vortex at the center of the chamber and the free-vortex zone at near the wall. The flow characteristics mentioned about during compression stroke showed the same as that found for previous paper (9) predicted using momentum equation. Further, regarding swirl chamber flow during expansion stroke, the maximum jet flow from the chamber during expansion stroke can be seen at about 200 deg.CA. After a time swirling flow decreases, and reverse-swirling flow appears in a part of the chamber at about 270 deg.CA.

The turbulence intensity I_t, defined by the dimensionless value $\sqrt{2k/3}/Cm$, at specified locations $\ell - \ell'$ shown in Fig.1 for various crank angles was computed and is shown in Fig.5. Where k is turbulence kinetic energy m^2/s^2, and Cm is mean piston velocity m/s. Turbulence intensity is very low at the beginning of the compression stroke, as shown in Fig.5(a). After crank angle reaches 50 degrees, intensity increases rapidly during compression and at about 130 deg.CA comparatively high turbulence intensities appear in the enter of the chamber and near the wall, and intensities decrease at 180 deg.CA. It is found that at 180 deg.CA a large value can be seen near the chamber wall and center due to high shear stresses generated in these regions and the minimum value occurs at nearly midway between chamber wall and center. Moreover, as shown in Fig.5(b), turbulence intensity decreases during expansion stroke except the center of the chamber.

Experiment was performed using the special air model of swirl chamber type A. The comparison was made between the experimental results and the simulations. The measured tangential velocity at the locations $\ell - \ell'$ shown in Fig.1 versus crank angle during compression stroke is shown in Fig.6 (a). Being seen in Fig.6(a), as the crank angle proceeds, the swirl velocity increases, and the swirl becomes alike a rigid-body rotation except the part close to the chamber wall. Decelaration near the wall was noticed during the compression stroke. On comparing the computed results in Fig.3 and Fig.4 with the measured values in Fig.6(a),it may be stated that the computed tangential velocity profiles during the compression stroke are comparatively good agreement with the experimental results. However, comparing the both velocity profiles in detail, a discrepancy was noticed midway between the center and the wall of the chamber at near TDC.

Further, from Fig.5 and Fig.6(b), it might be stated that, although predicted results for turbulence intensity are comparatively smaller than experimental results, the shifting of turbulence intensities at crank angles shows the same tendency with both cases.

Engine used in prediction. Next, simulations were attempted for an engine used in prediction, specifications for which are shown in Table 3. Computations were carried out for two types B and C of swirl chamber shapes which might be important in usual cases. Velocity fields computed from the beginning of compression to the end of expansion stroke for each swirl chamber are shown in Fig.7, Fig.8, Fig.10 and Fig.11.

In general, formation of swirl during compression stroke is similar to that observed in the air model. However, some differences exist in the profile of each swirl chamber shape. Referring to the flow in the swirl chamber during compression stroke, swirling flow of type C is stronger than that of tpye B, and velocity vectors of type B during expansion stroke are larger than that of

type C in the periphery. Specially, at 270 deg.CA, the flow in the chamber of type B increases near the passage in consequence of the ejected air flow from the chamber, while that of type C affected by the connecting passage and the bottom surface of the chamber is remarkable in the center of the chamber. At the end of the expansion stroke, the weak reverse-swirling flow is noticed in a part of the chamber with both types.

Finally, as shown in Fig.9 and Fig.12, the difference of turbulence intensity between both types can be found that the turbulence intensity of type C is comparatively larger than that of type B in the center of the chamber and near the wall during compression stroke, and the former still remains comparatively large turbulence in the center of the chamber at the end of the expansion stroke.

Computations for the above simulation were performed on FACOM M-360 computer in Himeji Institute of Technology.

CONCLUSIONS

The followings were concluded based on the predictions and experimental data obtained in this study.

1. Predicted tangential velocity and turbulence intensity qualitatively agreed with experimental results obtained using a special air model.
2. Prediction shows that during the compression stroke the turbulence intensity increases rapidly as tangential velocity increases.
3. Swirl chamber geometry greatly affectes turbulence intensity in the center of the chamber and near the wall, where turbulence intensity is strong.
4. During expansion stroke the swirl motion quickly decays, forming a reverse-swirling in the final stage.

ACKNOWLEDGEMENT

The authors would like to express their gratitude to Professor M. IKEGAMI, Kyoto University, Professor K. NISHIWAKI, Ritsumeikan University, and to Professor Y. HOSOKAWA, Himeji Institute of Technology for their most helpful advice. Thanks are also due to Mr. S. MATSUMOTO, student of Himeji Institute of Technology, for his laboratory work.

REFERENCES

1. Gosman,A.D., Johns,R.J.R., and Watkins,A.P., "Development of Prediction Method for In-Cylinder Processes in Reciprocating Engines," Combustion Modeling in Reciprocating Engines, (Mattavi,J.N.and Amann,C.A. ed.) Plenum Press, New York, pp.69-129, 1980.
2. Ramos,J.I., Humphrey,A.C., and Sirignano,W.A., "Numerical Prediction of Axisymmetric Laminar and Turbulent Flows in Motored, Reciprocating Internal Combustion Engines," SAE Paper No. 790356, 1979.
3. Elkotob,M.M., Abou-Ellail,M.M.M., and Salem, I.S., "Rotating Flow and Nonisotropic Turbulence in Reciprocating Engines," ASME Winter Annual Meeting of the Fluid Engineering Division, November 1982.
4. Ikegami,M., Komatsu,G., and Nishiwaki,K., "Numerical Simulation of Flow in an Engine Cylinder: 1st Report, Formulation and Algorithm," (in Japanese), Transactions of the Japan Society of Mechanical Engineers(B), Vol.51, No.466, pp. 1933-1940. 1985.
5. Nishiwaki,K., Komatsu,G., and Ikegami,M., "Numerical Prediction of Fluid Motion in an Internal Combustion Engine During Intake Process," (in Japanese), 4th JSME-JSAE Joint Symposium on Internal Combustion Engines, Proceedings, pp.49-54, 1984.
6. Wakisaka,T., Shimamoto,Y., Ishiki,Y.,and Shibata, "Simulation of Intake Process in a Four Cycle Engines," (in Japanese), 4th JSME-JSAE Joint Symposium on Internal Combustion Engines, Proceedings, pp.55-60, 1984.
7. Jones,W.P., and Launder,B.E., "The Prediction of Turbulence," Int. Jour. of Heat and Mass Trans., Vol.15, pp.301-314. 1972.
8. Patankar,S.V., "Numerical Heat Transfer and Fluid Flow," McGraw-Hill, pp.88-90, 1980.
9. Komatsu,G., Ikegami,M., "Numerical Simulation of Swirl Chamber Flow in Diesel Engines," (in Japanese), 5th JSME-JSAE Joint Symposium on Internal Combustion Engines, Proceedings, pp.1-6, 1985.

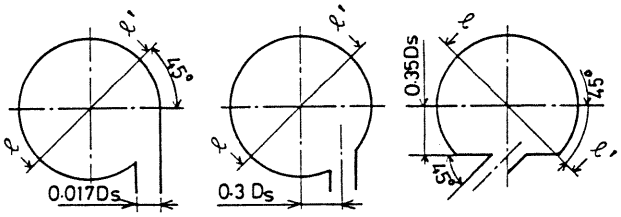

Type A Type B Type C

Fig. 1 Scheme of swirl chamber shapes

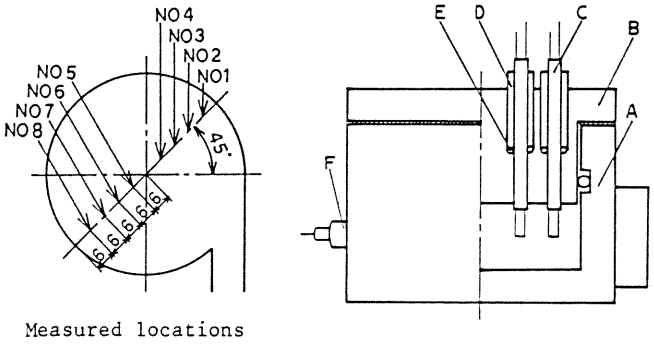

A Swirl chamber
B Cover
C Hot-Wire probe
D Set screw
E O ring
F Pressur transducer

Measured locations

Fig. 2 Schematic of experimental apparatus

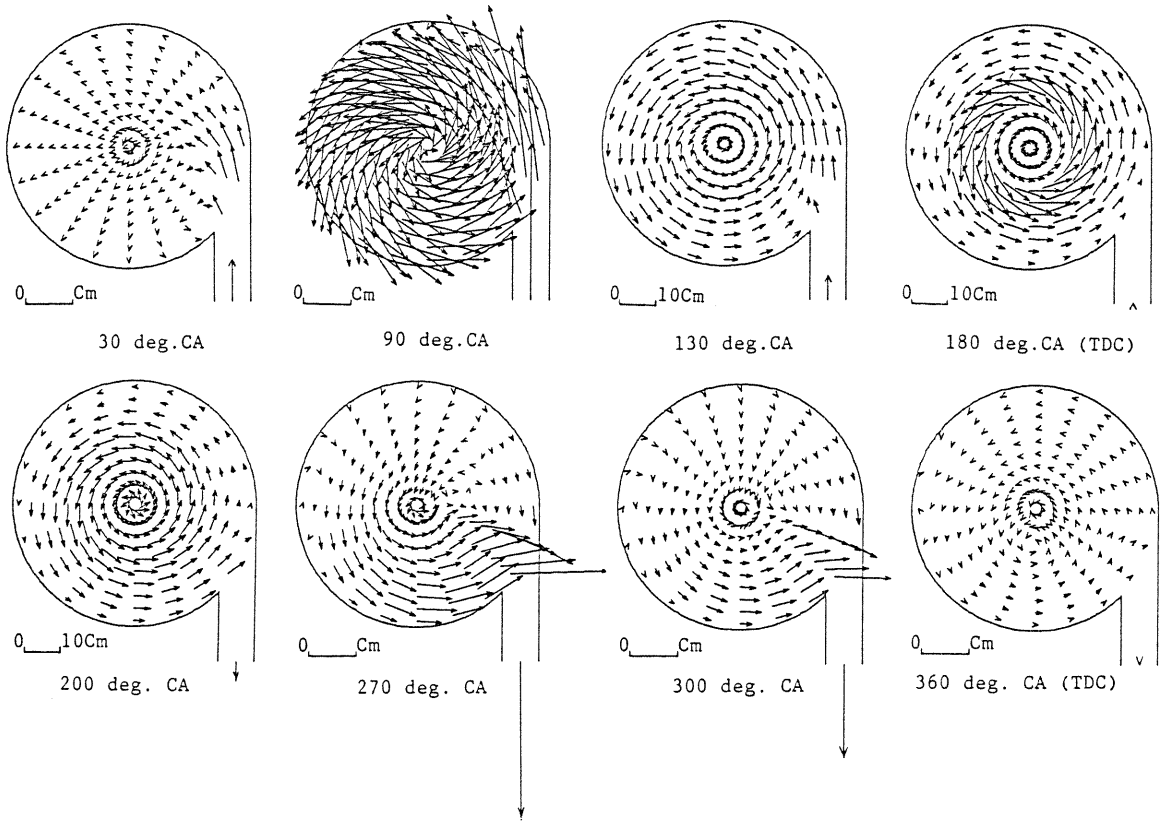

Fig. 3 Computed velocity fields during compression and expansion strokes for special air model

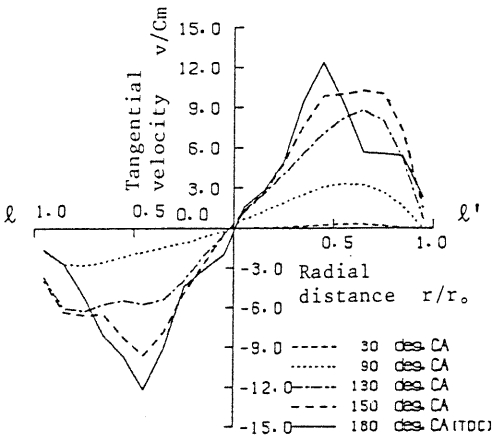

Fig. 4 Computed tangential velocity versus radial position at various crank angles for special air model

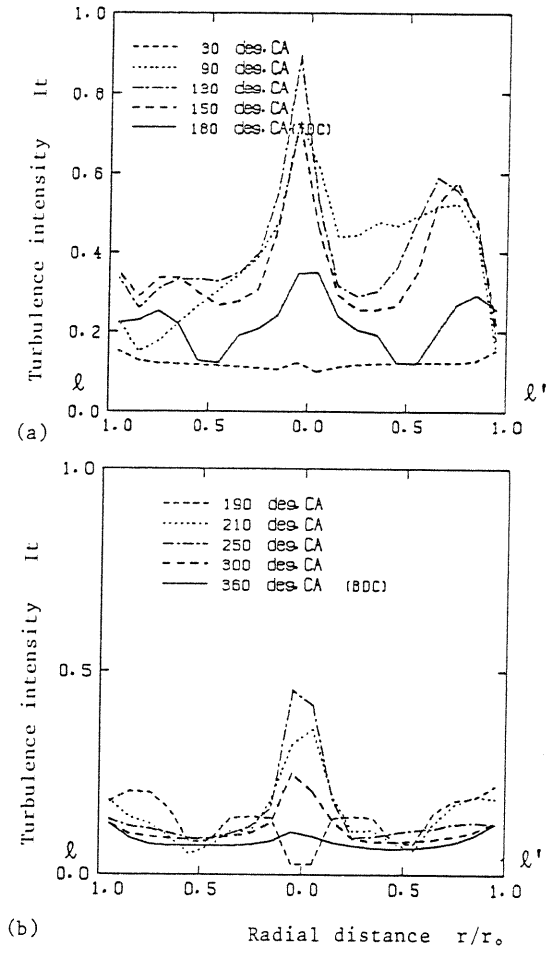

Fig. 5 Computed turbulence intensity versus radial position at various crank angles for special air model

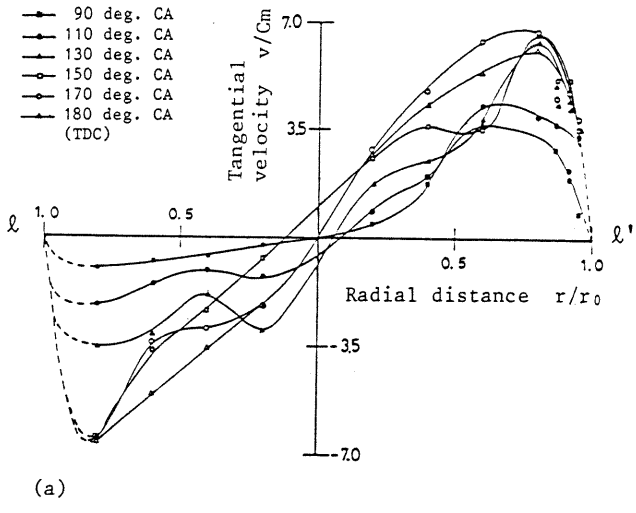

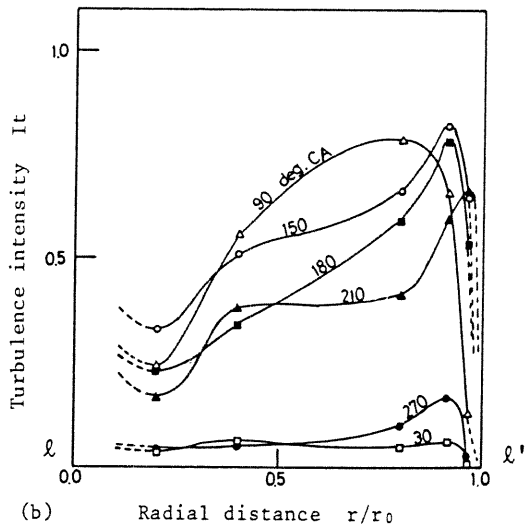

Fig. 6 Measured tangential velocity and turbulence intensity versus radial position at versus crank angles for special air model

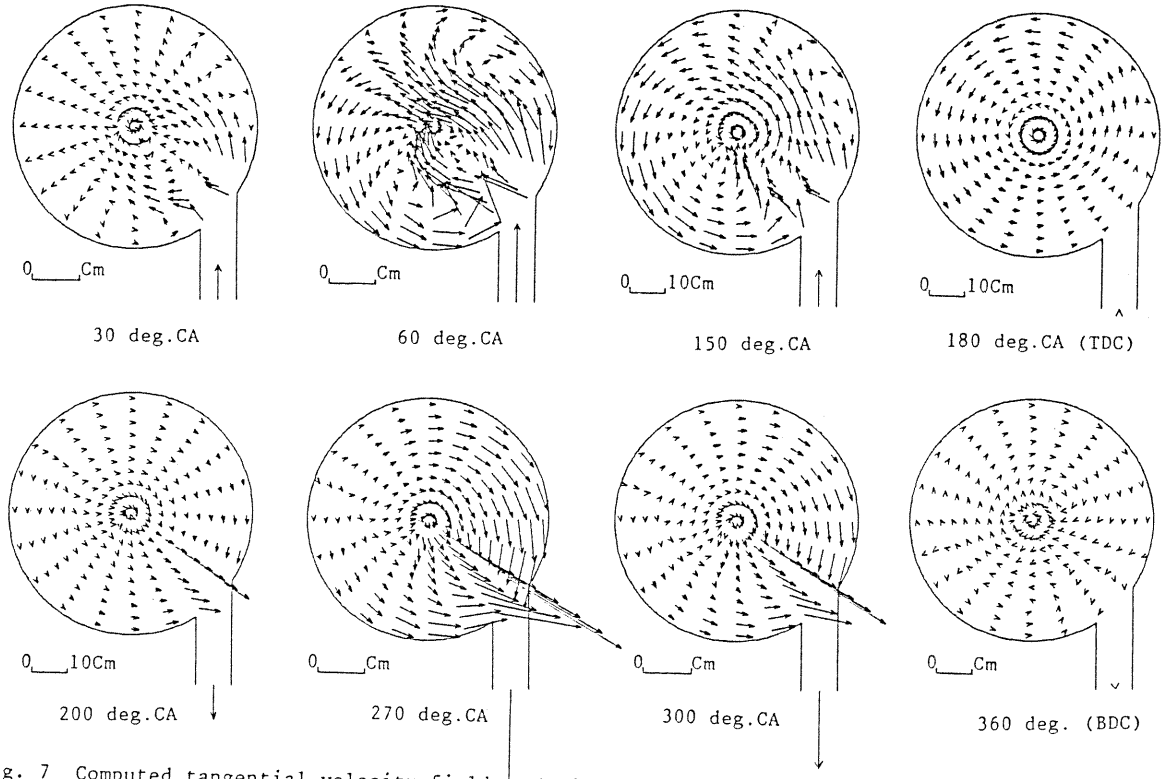

Fig. 7 Computed tangential velocity fields during compression and expansion stroke for swirl chamber shape B of engine used in prediction

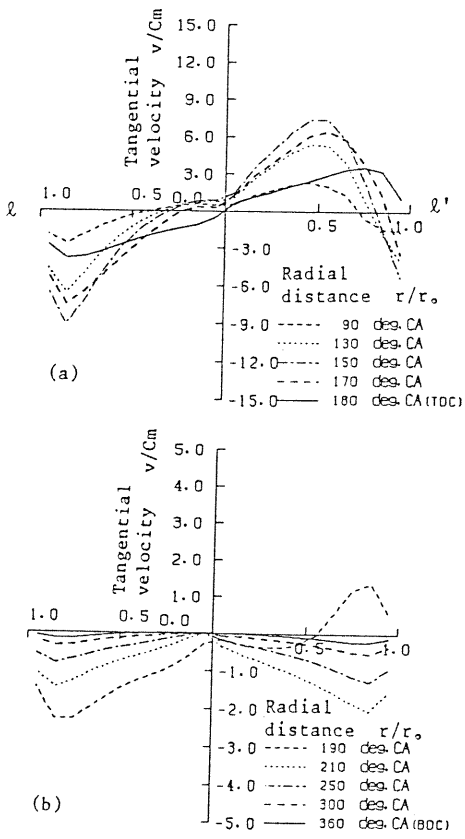

Fig. 8 Computed tangential velocity for swirl chamber shape B

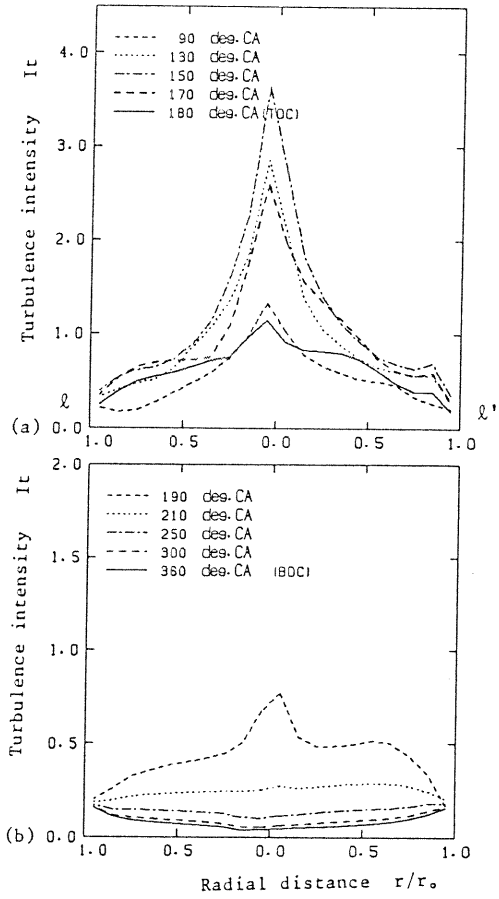

Fig. 9 Computed turbulence intensity for swirl chamber shape B

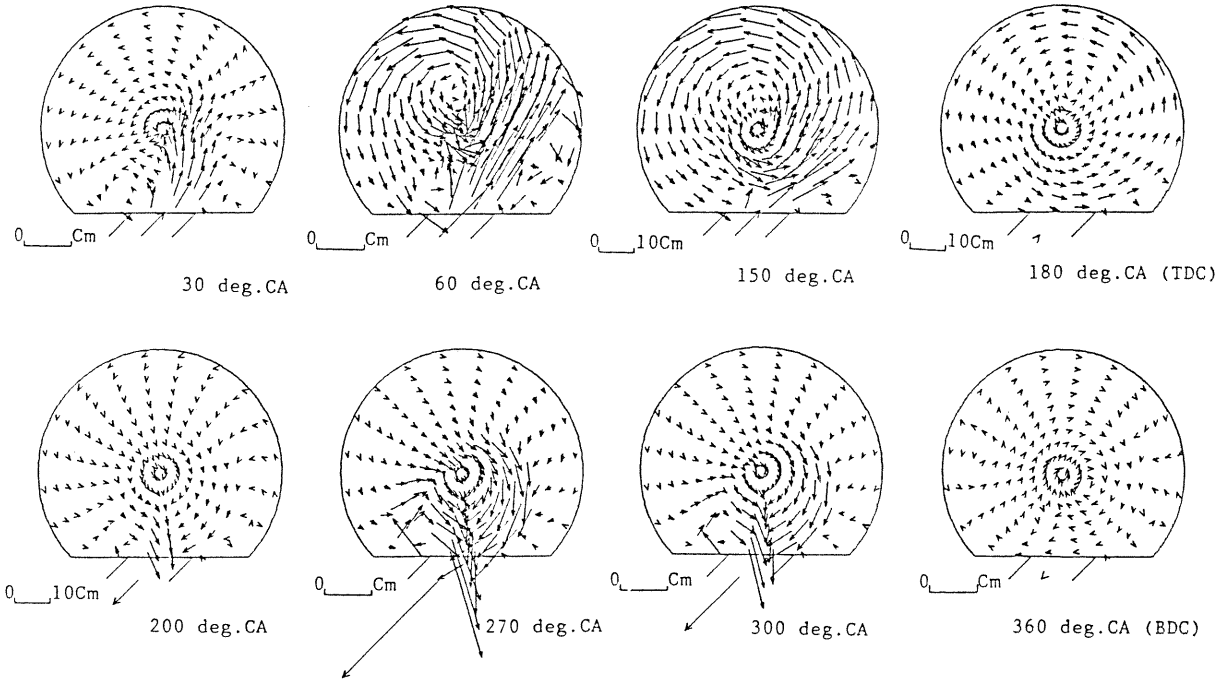

Fig. 10 Computed tangential velocity fields during compression and expansion for swirl chamber shape C of engine used in prediction

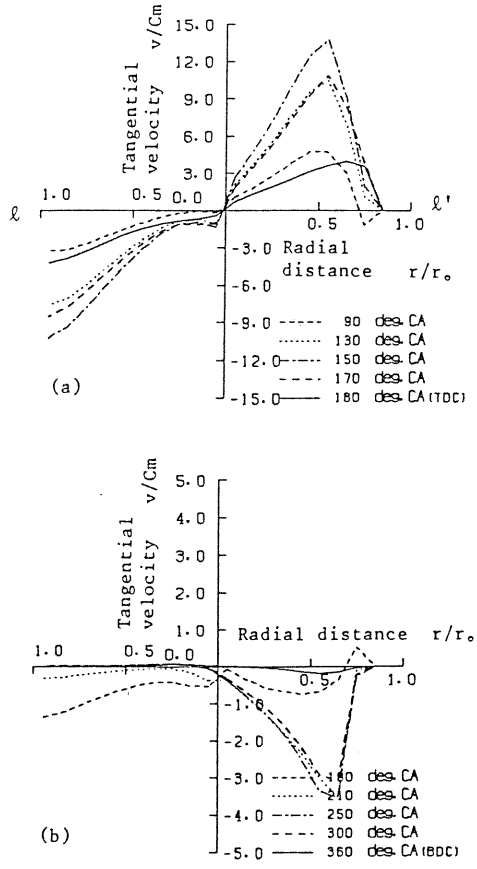

Fig. 11 Computed tangential velocity for swirl chamber shape C

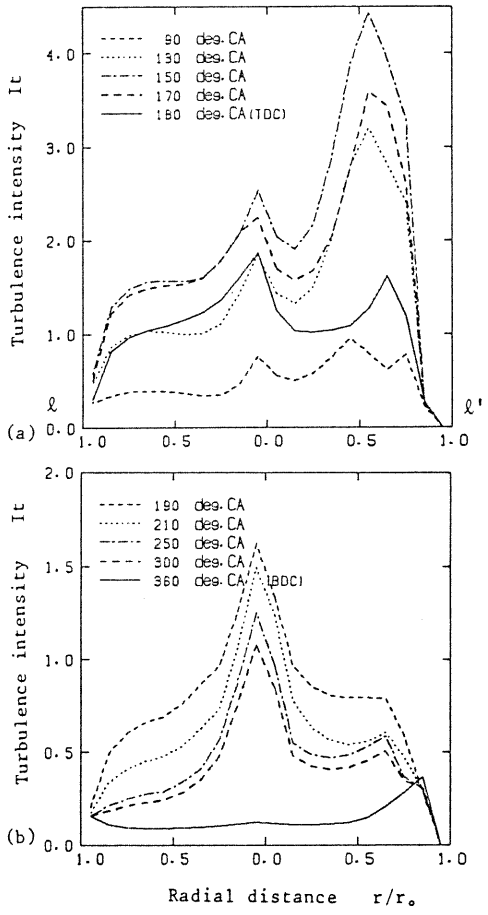

Fig. 12 Computed turbulence intensity for swirl chamber shape C